European Journal of Mechanics / B Fluids 67 (2018) 15–24

Contents lists available at ScienceDirect

European Journal of Mechanics / B Fluids

journal homepage: www.elsevier.com/locate/ejmflu

Analysis of Near-wall effect on cloud cavitating flow that surrounds an axisymmetric projectile using large eddy simulation with Cartesian cut-cell mesh method

Chang Xu, Yiwei Wang *, Chenguang Huang, Chao Yu, Jian Huang

Key Laboratory for Mechanics in Fluid Solid Coupling Systems, Institute of Mechanics, Chinese Academy of Sciences, Beijing, 100190, China
School of Engineering Science, University of Chinese Academy of Sciences, Beijing, 100049, China

ARTICLE INFO

Article history:
Received 18 October 2016
Received in revised form 18 April 2017
Accepted 2 July 2017
Available online 19 July 2017

Keywords:
Cloud cavitating flow
Near-wall effect
Large eddy simulation
Cartesian cut-cell mesh
Vortex structure

ABSTRACT

Near-wall effect is important for cavitation of flow and vortex structures. These structures are commonly investigated in cavitation of tip-vortex leakage, but are rarely discussed in cloud cavitating flow. In this study, typical experiments and numerical simulation of cloud cavitating flow were conducted near a wall that surrounds an underwater axisymmetric projectile. The experimental observations of cavity development are consistent with numerical results and validate the method's accuracy. Changes in the cavity of the distal and near wall side differ throughout the entire evolution process. The cavity grows faster on the near wall side than on the distal side, whereas the re-entry jet inside the cavity moves slowly toward the shoulder of the model. The strong vortex around the projectile is non-axisymmetric because of the collapsing cavity, which may also affect the cruising stability.

1. Introduction

Unsteady cavitating flow around high-speed underwater vehicles is one of the highly discussed topics in the engineering community [1,2]. Such unsteadiness causes serious consequences, e.g. noises, erosion, vibration and instability in trajectory. The near-wall effect is an important factor in the evolution of complex unsteady cavity evolution. For example, a two-dimensional cavitating flow cannot be easily generated in water tunnels because of sidewall effect. Therefore, the mechanism involved should be investigated to find solutions on controlling such effect in engineering applications.

Studying the effects of wall nearby on cavitation requires complex simulation and test equipment. Given this requirement, a limited number of research has explored this issue. Ishida and Kimoto conducted experimental analysis of the behavior of a single cavitation bubble near a wall to examine cavitation bubbles near a solid boundary using a quite complex test facility [3,4]. Zhou and Chen conducted a comparative study of ventilated supercavity around models with different shapes between the near-wall area and infinite flow [5–7] to explore near-wall effect. Wind tunnel test and CFD simulation were also conducted. He and Kida [8–10] studied near wall effect on supercavitating jet-flapped foils. Other studies focused on the interaction between free surface and cloud cavitating flow; these studies employed simulation methods, such as potential flow theory [11,12], boundary element method (BEM) [13–15] and large eddy simulation (LES) [16].

Most researchers focus on underwater cloud cavitating flow while neglecting wall effect. Experimental and numerical methods are usually used to analyze such problems. Traditional experimental methods include water tank test [17] and water tunnel test [18]. The CFD simulation method has also become increasingly popular in solving hydrodynamic problems; the tools adopted for this method include commercial [19,20], open-source [21,22] and in-house [23–25] software. Typical problems include cavitating flow of unsteady cloud around airfoil [26] and propeller models [27]. For axisymmetric projectile, an early simulation of steady and ventilated cloud cavitating flow around an underwater vehicle was demonstrated by Kunz [28]. Owis showed the cavity evolution of cavitating flow of an unsteady cloud around the same kind of vehicle [29]. Wang determined the relationship between the speed and position of a re-entry jet and adverse pressure gradient. The results of these studies can be used to predict the speed and cavity length of re-entry jets [30].

Good orthogonality and meshing quality is beneficial to the convergence of the calculation and the interface of high-precision capture, which are very important for the large eddy simulation. Fine mesh resolution is important for the LES of cloud cavitating flow, whereas cell size could substantially affect the simulation results and detailed phenomenon of cavity length [31]. For this

* Corresponding author at: Key Laboratory for Mechanics in Fluid Solid Coupling Systems, Institute of Mechanics, Chinese Academy of Sciences, Beijing, 100190, China.
E-mail address: wangyw@imech.ac.cn (Y. Wang).

http://dx.doi.org/10.1016/j.euromechflu.2017.07.001
0997-7546/

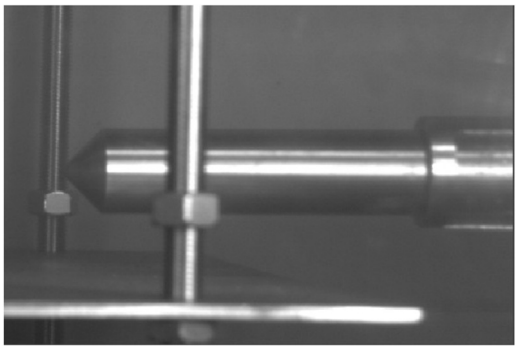

Fig. 1. Water tank test facility.

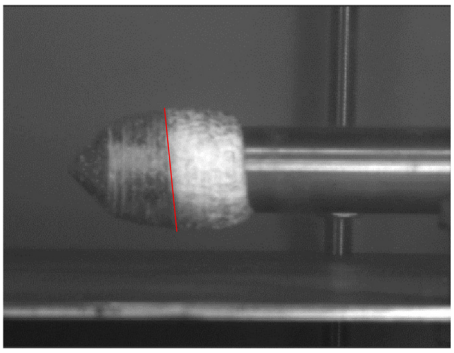

Fig. 2. Typical cavitation at $t = 0.006$ s. The white foam like re-entry jet inside the cavity is marked by a red line. (For interpretation of the references to color in this figure legend, the reader is referred to the web version of this article.)

reason, hexahedral mesh is usually used in the large eddy simulation. However, the structured mesh is difficult to generate for complex geometries, and the number of cells generated is quite large. Therefore, the application of structured grid will actually make the large eddy simulation more time-consuming. The Cartesian cut-cell method is an effective approach for generating unstructured mesh. This approach has underwent significant development in recent years. This approach easily achieves local refinement and perfect orthogonality and is suitable for complex geometries [32,33]. Despite this result, the application of Cartesian cut-cell meshes on unsteady cavitating flow requires further evaluation.

This study mainly involves two parts, namely, water tank test and CFD simulation. The evolution process of the cavity is recorded by a high-speed camera. Instead of using a typical structured mesh, simulation is based on LES, volume-of-fluid approach, and Cartesian cut-cell method for finite volume mesh generation. To facilitate validation, changes in cavity length are compared between that in the experiment and in CFD simulation. Mesh independence is also discussed. The key features of cavitating flow, re-entry jet, cavity shedding, cavity collapse, and the effect of the wall nearby on cavitating flow are analyzed. Consistent regularity is observed between the cavity and vortex motion.

2. Water tank experiment

2.1. Description of test facility

Fig. 1 shows the facility for water tank test used in the experiment. The model used is a steel cylinder with conical head. The longitudinal section of the cone is an isosceles right triangle. The model measures 200 mm × 37 mm × 37 mm, and the distance between the near wall side of the model and the wall nearby is 25 mm. Split Hopkinson pressure bar technology [17] is used as a launching source under typical conditions. Initially, the model is instantly accelerated to about 20 m/s and launched into a 1 m × 1 m × 2 m water tank. The temperature of the water inside the tank is about 20 °C. The entire experiment is recorded by a high-speed camera with a sampling frequency of 12 000 frames per second.

2.2. Typical experiment results and analysis

Fig. 2 shows a typical cavitation photograph at $t = 0.006$ s. Cavitating flow at this point developed into a stable shape. The white foam like re-entry jet inside the cavitating flow moves toward the leading edge of the model is marked by red line. As shown in the figure, the location of the near re-entry jet moves away from the front end of the model as the near wall side of the model approaches the wall nearby. The location of cavity length and re-entry jet at the distal and near wall side of the model can be measured from the figures. Cavity evolution includes cavity growth, cavity shedding, and cavity collapse. This phenomenon can be observed to validate the accuracy of the CFD simulation method in the next step.

The effect of resistance on the speed of the launched model is noticeable during experiment. The launch speed of the model at the beginning and end of the test can be derived from change of leading edge location of the model in the adjacent images, which is about 20 m/s. Cavitation number can be calculated using the following equation:

$$\sigma = \frac{p_\infty - p_v}{\frac{1}{2}\rho_l v_\infty^2} = 0.495 \tag{1}$$

where p_∞ is standard atmospheric pressure, p_v is saturated vapor pressure, ρ_l is liquid water density, and v_∞ is launch speed. The pressure inside the cavity which should be lower than the saturated pressure of water is considered as the cavitation criterion in the paper. There also exist other algorithm which may take the expression of the turbulent kinetic energy of 0.5 pk as a supplement to the saturated pressure, with reference to the Singhal model [34]. For the problem discussed in this paper, the turbulence of the incoming flow is quite low. The turbulence to the saturated pressure caused by the turbulent kinetic energy and the saturated pressure are relatively small comparing to the background pressure and the flow pressure. Small changes of the saturated pressure will not affect the cavitating flow much. The cavitation number in this paper remain constant as the model speed as well as the saturated vapor pressure of water did not change during the experiment. J. H. Kim [35] and D. R. Stinebring [36] discuss the relationship between the cavitation and the cavitation number in details. Given that the model is small and fast, the difference between the pressure exerted by gravity at the distal and near wall side of the model is nearer than flow dynamic pressure. The equation $\frac{\rho_l g d}{\frac{1}{2}\rho_l v_\infty^2} = 0.0018 \ll 1$ shows that variation of local cavitation number in y direction is very small. $d = 37$ mm is the projectile diameter.

3. Numerical method

3.1. Governing equations

Multiphase flow equations are widely used to describe water-liquid/water-vapor two phases flow problems. The governing equations are,

$$\frac{\partial \rho}{\partial t} + \frac{\partial \left(\rho u_j\right)}{\partial x_j} = 0 \tag{2}$$

$$\frac{\partial(\rho u_i)}{\partial t} + \frac{\partial(\rho u_i u_j)}{\partial x_j} = -\frac{\partial p}{\partial x_j} + \frac{\partial}{\partial x_j}\left(\mu \frac{\partial u_j}{\partial x_j}\right) \tag{3}$$

where u_i is velocity component in i direction, ρ is the mixture density, p is pressure, μ is the laminar viscosity which can be defined as,

$$\mu = (1-\alpha_v)\mu_l + \alpha_v \mu_v \tag{4}$$

where α is the volume fraction of the different phases, l and v represent liquid water and water vapor. The mixture density ρ is defined as,

$$\rho = (1-\alpha_v)\rho_l + \alpha_v \rho_v. \tag{5}$$

The transport equation of the water vapor volume fraction is,

$$\frac{\partial(\alpha_v \rho_v)}{\partial t} + \frac{\partial(\alpha_v \rho_v u_j)}{\partial x_j} = \dot{m}^+ - \dot{m}^- \tag{6}$$

where $\dot{m}^+$ and $\dot{m}^-$ are the mass transfer rate of evaporation and condensation, derived from the Reyleigh–Plesset bubble dynamics equations by Zwart et al. [37].

$$\dot{m}^+ = F_{vap}\frac{3a_{nuc}(1-\alpha_v)\rho_v}{R_B}\sqrt{\frac{2}{3}\frac{max(p_v - p, 0)}{\rho_l}} \tag{7}$$

$$\dot{m}^- = F_{cond}\frac{3\alpha_v \rho_v}{R_B}\sqrt{\frac{2}{3}\frac{max(p - p_v, 0)}{\rho_l}} \tag{8}$$

where $R_B = 10^{-6}$ m is the generalized bubble radius, $p_v = 2340$ Pa is the saturated vapor pressure, $a_{nuc} = 5 \times 10^{-4}$ is the nucleation site volume fraction, $F_{vap} = 50$ is the evaporation coefficient, $F_{cond} = 0.01$ is the condensation coefficient. The chose parameter values are based on the work of Zwart et al. The parameters have been discussed and found to work well for a variety of fluids and devices. The parameters and the recommended value of the cavitation model are widely used [16]. Besides, some studies have shown that within a certain range, the parameters have little effect on the results of cloud cavitating flow [38].

3.2. LES approach

LES equations are derived from the above Eqs. (2) and (3) by applying a Favre-filtering operation,

$$\frac{\partial \rho}{\partial t} + \frac{\partial(\rho \bar{u}_j)}{\partial x_j} = 0 \tag{9}$$

$$\frac{\partial(\rho \bar{u}_i)}{\partial t} + \frac{\partial(\rho \bar{u}_i \bar{u}_j)}{\partial x_j} = -\frac{\partial \bar{p}}{\partial x_j} + \frac{\partial}{\partial x_j}\left(\mu \frac{\partial \bar{u}_j}{\partial x_j}\right) - \frac{\partial \tau_{ij}}{\partial x_j} \tag{10}$$

where τ_{ij} is the subgrid scale (SGS) stress, which is defined as,

$$\tau_{ij} = \rho\left(\overline{u_i u_j} - \bar{u}_i \bar{u}_j\right). \tag{11}$$

Based on the Boussinesq equation, the SGS stress could be computed from,

$$\tau_{ij} - \frac{1}{3}\tau_{kk}\delta_{ij} = -2\mu_t \bar{S}_{ij} \tag{12}$$

where μ_t is the eddy viscosity, τ_{kk} is the isotropic part, $\bar{S}_{ij}$ is the rate-of-strain which is defined as,

$$\bar{S}_{ij} \equiv \frac{1}{2}\left(\frac{\partial \bar{u}_i}{\partial x_j} + \frac{\partial \bar{u}_j}{\partial x_i}\right). \tag{13}$$

In the WALE model the eddy viscosity is modeled by,

$$\mu_t = \rho \Delta_s^2 \frac{\left(S_{ij}^d S_{ij}^d\right)^{3/2}}{\left(\bar{S}_{ij}\bar{S}_{ij}\right)^{5/2} + \left(S_{ij}^d S_{ij}^d\right)^{5/4}} \tag{14}$$

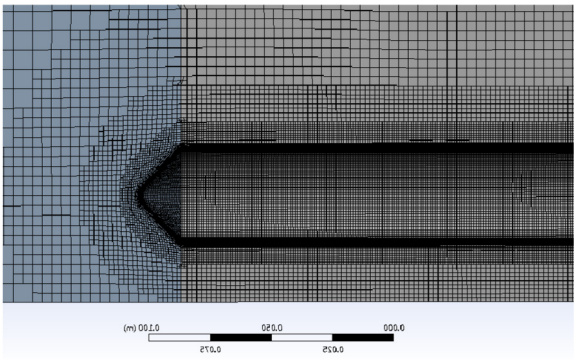

Fig. 3. Cartesian cut-cell mesh around the projectile. The total cell number is about 300 million.

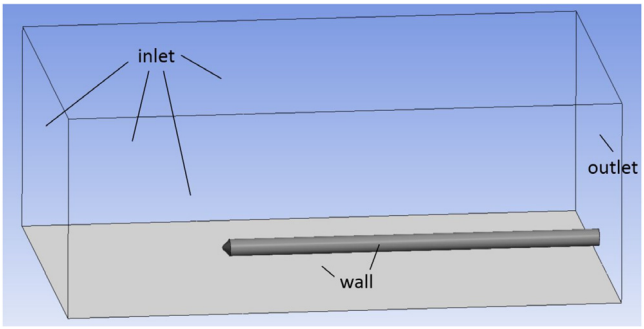

Fig. 4. Calculated domain and boundary conditions. The defined velocity-inlet, pressure-outlet and wall boundary conditions are marked.

where $\Delta_s = C_w V^{1/3}$, $S_{ij}^d = \frac{1}{2}\left(\bar{g}_{ij}^2 + \bar{g}_{ij}^2\right) - \frac{1}{3}\delta_{ij}\bar{g}_{kk}^2$, $\bar{g}_{ij} = \frac{\partial \bar{u}_i}{\partial x_j}$, the constant $C_w = 0.325$.

3.3. Cartesian cut-cell mesh

A semi-infinite model is adopted to ignore the effect of projectile tail. Commercial software ANSYS Meshing is used to generate a Cartesian cut-cell mesh with 15 layers of inflation. The height of the first layer is set to 1×10^{-4} m with a growth rate of 1.1. The minimum face size of the model is 1×10^{-3} m. The figure shows that the spatial volume grids are composed of cubes of different sizes. The total cell number is about 300 million (see Fig. 3).

3.4. CFD simulation setups

Commercial software FLUENT is used to simulate cavitating flow near the wall of an underwater axisymmetric projectile. The defined velocity-inlet, pressure-outlet and wall boundary conditions are shown (see Fig. 4).

LES approach and the wall-adapting local-eddy viscosity (WALE) model are adopted to simulate turbulent flow. The other detailed numerical schemes and parameters are shown in Table 1. Second-order implicit scheme is used for time discretization, which is compatible with the cavitation model and LES method. The body force weighted option is selected for pressure interpolation. The modified high-resolution interface-capturing scheme selected is more robust than explicit geometric reconstruction scheme and compatible with cavitation mass transfer. As whole acceleration process is very short in the experiment, the unsteady cavitating flow simulations are started from a uniform flow field. The time step size is set as 10^{-5} s.

Table 1
Numerical schemes and parameters.

Scheme in time	Second-order implicit
Pressure interpolation	Body Force Weighted
Scheme in volume fraction	Modified HRIC
Inlet velocity	20 m/s
Time step size	1×10^{-5} s

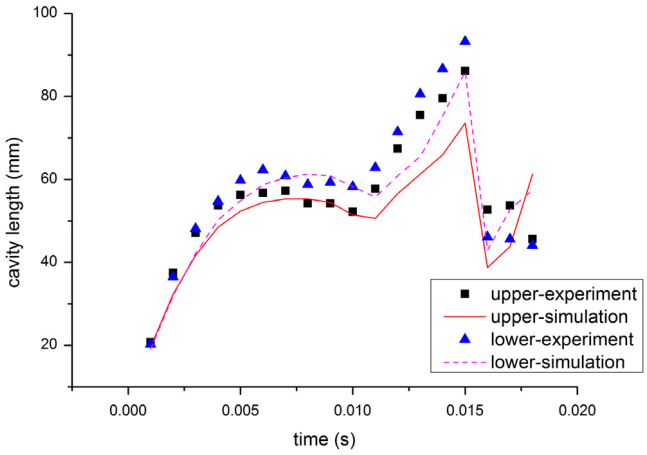

Fig. 5. Comparison of the cavity length at distal and near wall side between the experimental and simulated results.

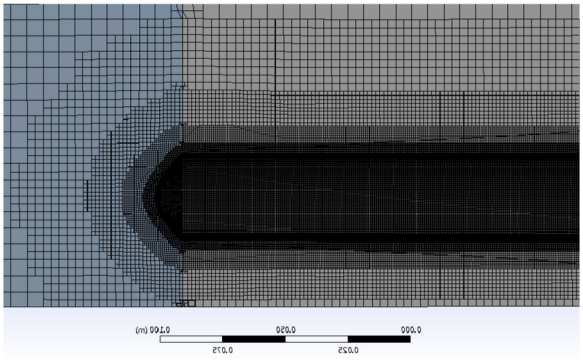

Fig. 6. Refined mesh of 1700 million cell number.

3.5. Validation

The cavity lengths at the distal and near wall side are compared in both experimental and simulated results to validate the accuracy of the simulation method (Fig. 5). Cavity evolution involves four stages of cavity development, namely, growth, re-entry, shedding, and collapse. Both the calculated cavity lengths on the upper and lower side of the projectile are smaller than the experimental data shown in the figure. This may due to the non-condensable gas in the cavitating flow during the experiment, which makes the cavity larger. Due to the limit of the solver, non-condensable gas or nucleation site cannot be considered in the calculation method. The simulation is reasonably accurate.

3.6. Mesh independence study

To verify the suitability of the original mesh size for the simulation, we produce a new refined mesh that contains about 1700 million cells. We use the same Cartesian cut-cell finite-volume approach (Fig. 6).

The resultant cavity lengths are compared between that in the previous simulation and in the experimental results. Fig. 7 shows

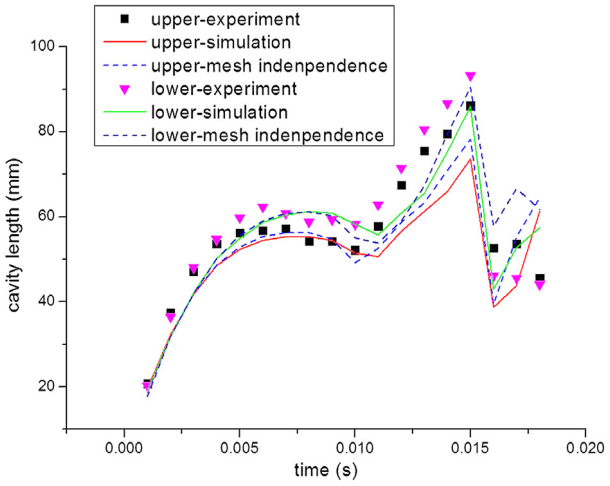

Fig. 7. Comparison of the cavity length at distal and near wall side between the experimental, original mesh and refined mesh simulated results.

the results. The new mesh plan generates more accurate results than the previous model. In the present study, we consider the main features of cavity evolution to a greater extent than in other attributes. By comparing the images shown in Fig. 8, we find that the refined mesh simulation results are consistent with the original results of cavity evolution. The features used for comparison include cavity length, re-entry jet fronts, and cavity shape. After verifying the mesh independence of the simulation method, the simulation results of the original mesh are used for further analysis and discussion. The results show that the Cartesian cut-cell mesh is fairly stable. The simulated results of small cell sizes remain fine.

The analysis indicates several advantages of the Cartesian cut-cell method. The most apparent benefit include rapid generation, which results in predominantly high-quality hexahedral elements and solver compatibility. The simulation method used in this study is stable.

3.7. Cavitation criterion

As mentioned above, the pressure inside the cavity which should be lower than the saturated pressure of water is considered as the cavitation criterion in the paper. To find how the results are dependent on the cavitation criterion, we compared the simulated results of the water temperature at 15, 20, 25 and 30 °C. The corresponding saturated pressure are 1700, 2340, 3170 and 4245 Pa. Comparisons of the cavity shape are shown in Fig. 9. From the results, we can find that small changes of the saturated pressure will not affect the cavitating flow a lot.

4. Results and discussion

4.1. Cavity evolution process

Cavity evolution involves four stages. Figs. 10–13 show the comparison of cavity images between the experimental and simulation results. The cavitating flow of the sheet evolves and grows at the first stage. Cavity length increases as growth rate decreases before reaching its peak. The re-entry jet inside the cavitating flow persistently moves toward the leading edge of the model. During this time, the shape of the cavity is stable. At the third stage, the re-entry jet inside the cavitating flow reaches the leading edge of the projectile and connects the outside flow and cavity shed. A new cavity begins to grow at this point and the previous cavity starts

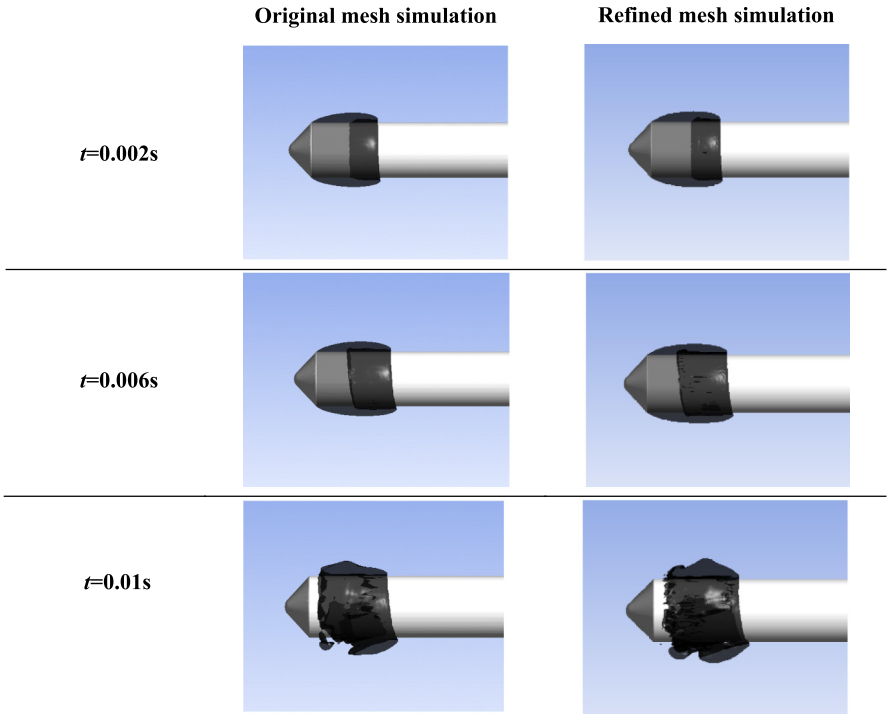

Fig. 8. Comparison of the cavity evolution between the original mesh and refined mesh simulated results.

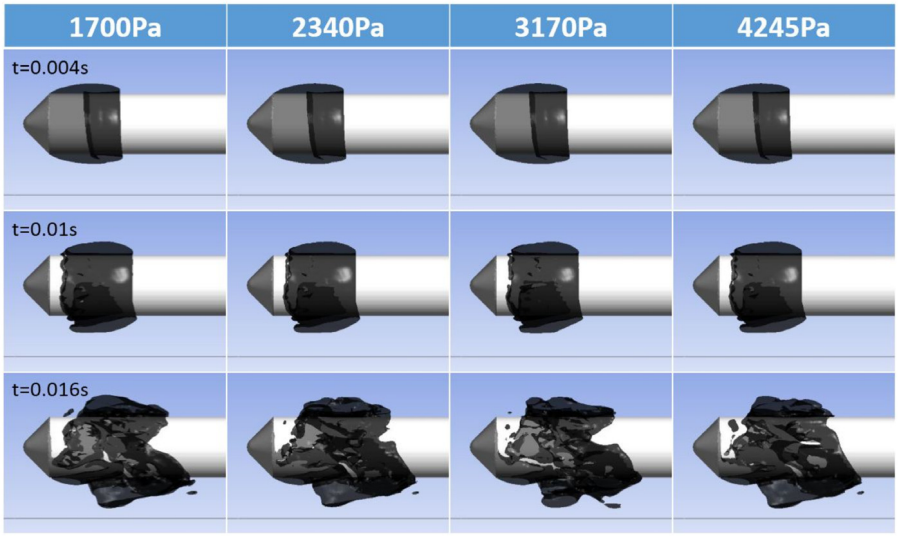

Fig. 9. Comparisons of the cavity shape when the saturated pressure of water are 1700, 2340, 3170 and 4245 Pa at $t = 0.004$ s, 0.01 s and 0.016 s.

to move downstream. These stages result in rapid growth of the length of total cavity. The cavity collapses at the closure in the last stage, and the length of cavity is drastically decreased. The growing cavity in the new cavity evolution process is then observed. This analysis shows that the re-entry jet inside the cavitating flow exerts a negligible influence on cavity evolution.

The characteristics of cavity evolution at the distal and near wall side at different stages are discussed. Fig. 10 shows the growth of cavity length. Two typical times at $t = 0.002$ s and $t = 0.004$ s are chosen for analysis. At $t = 0.004$ s, cavity length at the near wall side of the model is slightly longer than that of the distal side, but this difference is hardly noticeable.

The differences in cavity length and the front of re-entry jet between the distal and near wall side expands over time in the second stage as the re-entry jet inside the cavitating flow appears and continually moves toward the front end of the model. Re-entry jet inside the cavity are marked by red lines in the figure. Cavity length at the near wall side of the model is longer than that on the distal side, while the front of re-entry jet moves away from the leading edge of the cavity (Fig. 11). These stages are likely caused by the wall nearby because a low-pressure area is generated between the near wall side and the bottom wall (Fig. 16). The length and shape of total cavity are stable during this period. The re-entry jet is significant in cavity shedding. The velocity vector in the x direction around the model from the simulation results is shown at $t = 0.006$ s in Fig. 14. A cylindrical surface of 38 mm diameter is added to show the velocity of re-entry jet. The directions of opposite velocity vector divided by the edge of the cavitating flow could be clearly seen from the following figure. The cavity on the

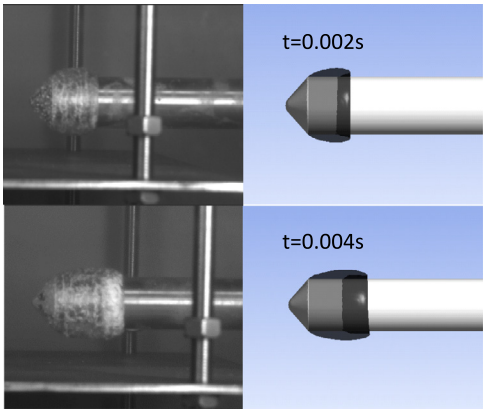

Fig. 10. Comparison of the cavity patterns between experiment and simulation results at $t = 0.002$ s and $t = 0.004$ s.

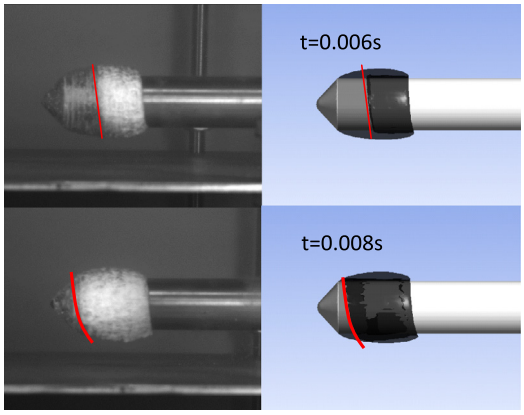

Fig. 11. Comparison of the cavity patterns between experiment and simulation results at $t = 0.006$ s and $t = 0.008$ s. (For interpretation of the references to color in this figure legend, the reader is referred to the web version of this article.)

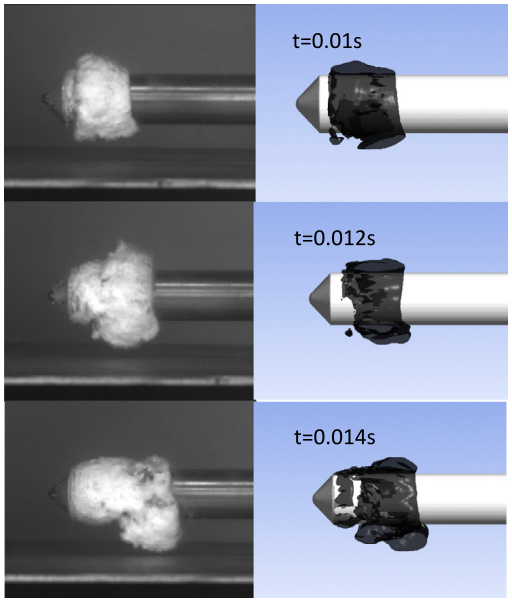

Fig. 12. Comparison of the cavity patterns between experiment and simulation results at $t = 0.01$ s, $t = 0.012$ s and $t = 0.014$ s.

distal side is cut off earlier than the cavity on the near wall side as the re-entry jet persistently moves upstream.

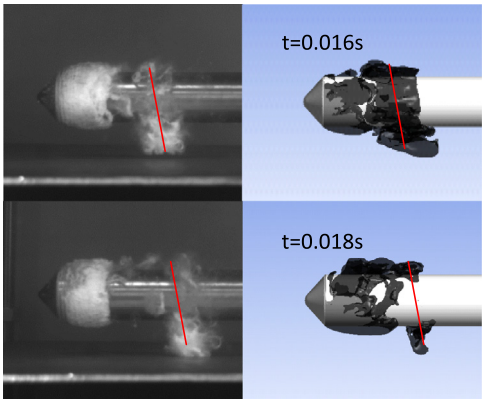

Fig. 13. Comparison of the cavity patterns between experiment and simulation results at $t = 0.016$ s and $t = 0.018$ s. (For interpretation of the references to color in this figure legend, the reader is referred to the web version of this article.)

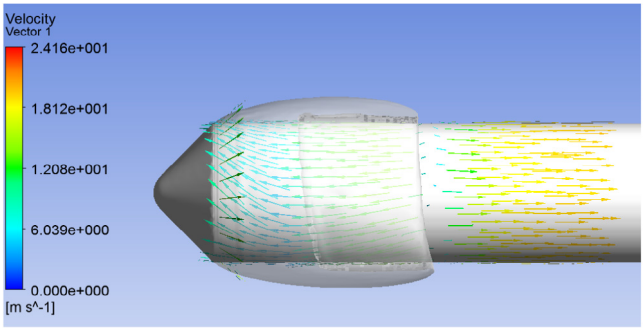

Fig. 14. Velocity vector in x direction at $t = 0.006$ s (on the surface of 38 mm diameters). The directions of opposite velocity vector divided by the edge of the cavitating flow can be observed.

Fig. 12 shows three images at corresponding time points ($t = 0.01$ s, 0.012 s, 0.014 s) during cavity shedding. The jet cuts off the cavity by interfering with the main flow as the re-entry jet moves to the shoulder of the projectile. The cavity generated in the first period sheds and the new cavity evolution process begins to grow. Total cavity length increases relative to those in the previous stages. The figure also shows that the thickness of the cavity at the near wall side of the model is thicker than that at the distal side. This result may be attributed to the larger low-pressure area at the near wall side than at the distal side to the wall because of the wall nearby. Velocity distribution around the model at the added neutral plane in this stage is shown in Fig. 15. The re-entry jet area inside the cavitating flow that moves toward the front end of the projectile is large at the near wall side and grows over time.

The cavity collapses at the last stage (Fig. 13). A comparison of the cavity images between experiment and simulation results at $t = 0.016$ s and $t = 0.018$ s shows that the cavity at the distal side collapsed first. The collapsing cavity is shown as an oblique line that begins from the left part of the distal side to the right part of the near wall side. Collapse at the near wall side of the model is delayed because of the effect of wall nearby. The cavity at the near part remains thicker in this stage than the distal part. A new cavity grows in the next cavity evolution period. Experiment results show that the newly generated cavity is not pure water vapor. The white foam like cavity means that the water content of it is quite high. As we used added iso-surface of water volume fraction = 0.5 to show the shape of the cavity, the newly generated cavity is not obvious. The new cavitation could be observed through the pressure contour chart (Fig. 16) shows the pressure distribution around the model. The low pressure area after the shoulder of the projectile actually shows the existence of new cavitation.

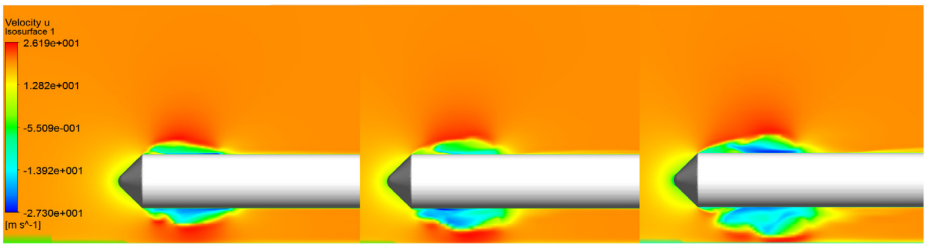

Fig. 15. Velocity contour charts at $t = 0.01$ s, $t = 0.012$ s and $t = 0.014$ s. Velocity distribution around the projectile is shown.

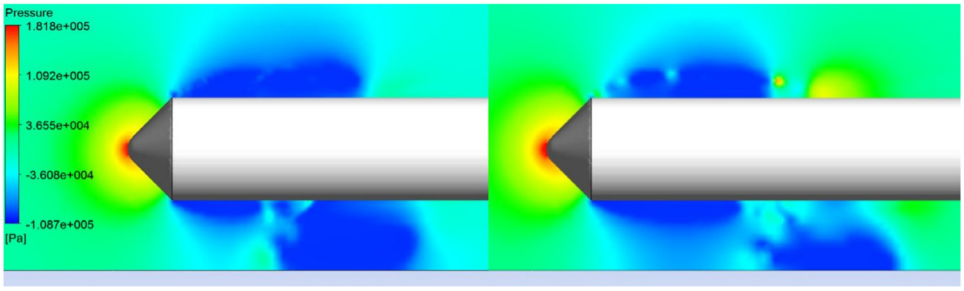

Fig. 16. Pressure contour charts at $t = 0.016$ s and $t = 0.018$ s. Pressure distribution around the projectile is shown.

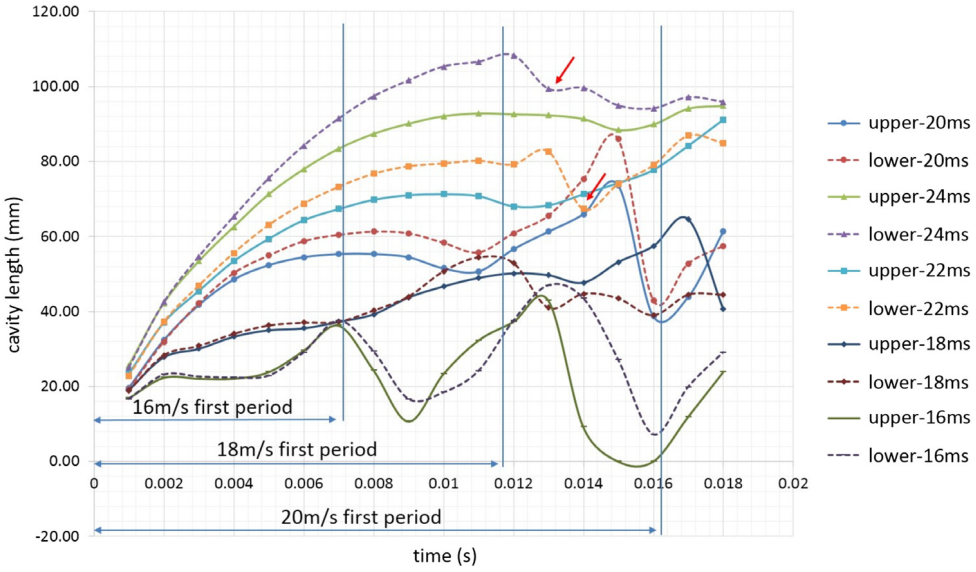

Fig. 17. Comparison of the cavity length on the distal and near sides to the wall when the model speed are 16, 18, 20, 22 and 24 m/s. First period as well as partial shedding cavities are marked.

4.2. Discussion of various cavitation numbers

To analyze the effect of cavitation number on the cavitating flow, we compared the simulated results when the model speed at 16, 18, 20, 22 and 24 m/s. The corresponding cavitation number are 0.773, 0.611, 0.495, 0.409 and 0.344. Results are shown in Fig. 17. It shows that partial shedding cavity on the lower side of the projectile near the wall occurs at 22 m/s and 24 m/s, when the cavity thickness close to the distance between the projectile and the wall. The reduction in cavitation number will not only increase the length and thickness of the upper and lower side cavity, increase the cavity evolution period, but also increase the thickness of the re-entry jet in the lower side cavity [26]. Growth of the cavity evolution period at various speed is regular. Each increased by 0.004 s. In a word, the cavitation number could affect the cavity shape as well as cavity evolution process.

Details of the cavitating flow of the simulated cases are compared in Fig. 18. The partial shedding cavity of the lower side cavity are pointed out by red arrow.

4.3. Near wall effect on cavity

4.3.1. Effect on cavity shape

Pressure distribution around the model at the added symmetry plane is shown at $t = 0.006$ s in Fig. 19. This approach was adopted to determine the factor that caused the difference between the cavity on the distal and near wall side to the wall. Two straight red lines are added to the near wall and distal side to the wall. Fig. 20 shows the distributed pressure along the lines.

The figures show that the low-pressure zone at the near wall side is longer than that at the distal side to the wall. The cavity on the distal side is short, which indicates that the constraint of the

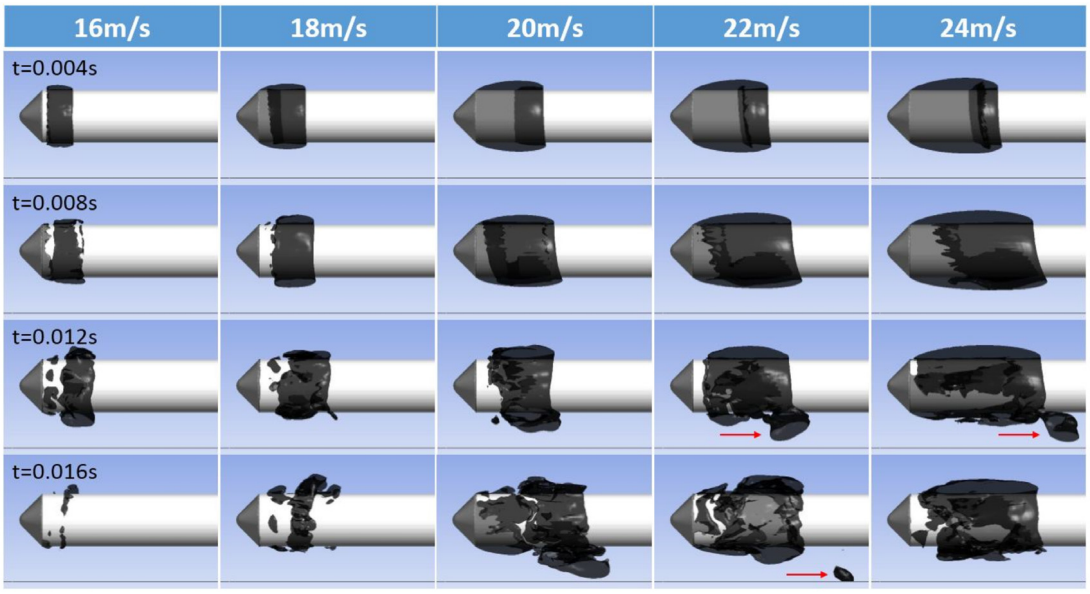

Fig. 18. The cavitating flow of the simulated cases when the model speed are 16, 18, 20, 22 and 24 m/s at $t = 0.004$ s, 0.008 s, 0.012 s and 0.016 s. Partial shedding cavity on the lower side of the projectile are pointed out by red arrows. (For interpretation of the references to color in this figure legend, the reader is referred to the web version of this article.)

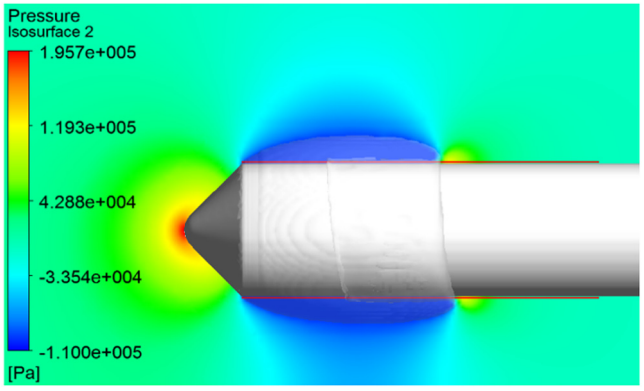

Fig. 19. Pressure contour chart at $t = 0.006$ s. Pressure distribution around the projectile is shown. Two straight red lines are added to the near wall and distal side to the wall. (For interpretation of the references to color in this figure legend, the reader is referred to the web version of this article.)

surrounding flow gains strength as it approaches the wall nearby. At $x = 0$ m, the pressure at the near wall side increases, which could decrease the cavitation number obtained in Eq. (1). Thus, cavity easily forms near the wall. As cavitation is the formation of vapor cavities in a liquid, the whole cavity evolution process is in a quasi-equilibrium state. Phase change from liquid water to vapor occurs in the region where the local pressure is lower than the saturated pressure, which is considered as the cavitation criterion in the paper. Pressure in the cavitation zone is constant, which equals to the saturated pressure of water mentioned in Section 3.1.

4.3.2. Effect on shedding vortex structures

The relationship between the shedding cavity and the vortex motion could be visualized based on the Q-criterion [39], which is defined by the following equation in incompressible flow:

$$Q = \frac{1}{2}\left(\|\Omega\|^2 - \|D\|^2\right) \tag{15}$$

where $\Omega = \frac{1}{2}\left(\nabla\vec{v} - \nabla\vec{v}^T\right)$ is the vorticity tensor, $D = \frac{1}{2}\left(\nabla\vec{v} + \nabla\vec{v}^T\right)$ is the strain rate tensor. Q has a direct physical interpretation. When $Q > 0$, the vector field is dominated by the

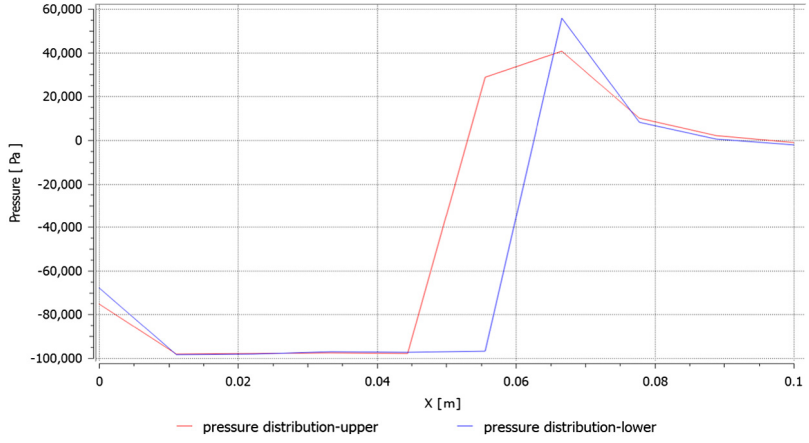

Fig. 20. Pressure distribution along the added lines at distal and near wall side of the model.

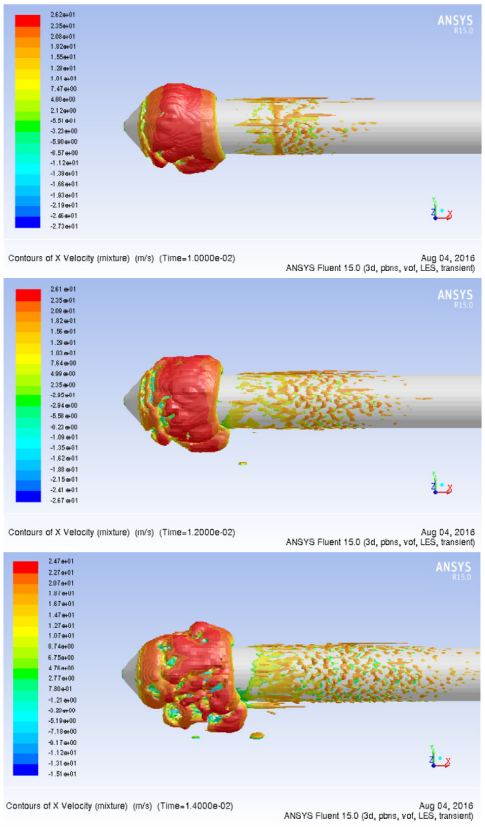

Fig. 21. Velocity distribution on the added iso-surface of $Q = 50000$ at $t = 0.01$ s, $t = 0.012$ s and $t = 0.014$ s.

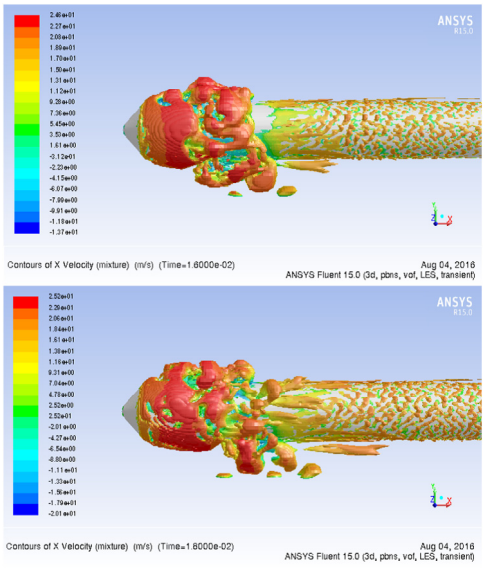

Fig. 22. Velocity distribution on the added iso-surface of $Q = 50000$ at $t = 0.016$ s and $t = 0.018$ s.

vorticity and the region is determined as a vortex tube. When $Q < 0$, the vector field is dominated by the strain. This physical interpretation supports the value of Q-criterion in the vector fields when areas of high strain and areas of strong vertical motions should be distinguished.

Velocity distribution on the added iso-surface of $Q = 50000$ is shown in Fig. 21 at $t = 0.01$ s, $t = 0.012$ s, and $t = 0.014$ s, and Fig. 22 at $t = 0.016$ s and $t = 0.018$ s. These figures contain the third and fourth stages of cavity evolution. The shedding vortex breaks up strongly induced by the collapse of the shedding cavity and the broken vortex is thick on the near wall side of the model because of the effect of the wall nearby. The non-axisymmetric vortex around the projectile caused by the collapse of the shedding cavity could produce a large lateral force and influence cruising stability.

5. Conclusions

This study uses water tank test and CFD simulation method to analyze cavitating flow near the wall around an underwater axisymmetric projectile. Cavity evolution includes cavity growth, re-entry jet, cavity shedding, and collapse. These processes are observed through experiment images and simulation. The comparison results of the cavity lengths at the distal and near wall sides to the wall between the experimental and numerical results show that the simulation method is reasonably accurate.

Cavity length at the near wall side of the model is longer than that at the distal side, whereas the front of re-entry jet move away from the leading edge of the cavity. Shedding cavity is thicker at the near wall side and collapses later under the effect of the wall nearby.

Re-entry jet is a highly important factor that induces instability. Adding a cylindrical surface to show the velocity streamlines around the projectile reveals the internal movement of re-entry jet toward the leading edge of the cavity. Velocity contour charts show velocity distribution on the neutral surface. The re-entry jet at the near wall side is thicker than that at the distal side. The effect of the wall nearby is also analyzed. The constraint of the surrounding flow is strong when the bottom wall is near, which could be concluded from the pressure contour chart around the projectile. Pressure distribution along the added lines at the distal and near wall side of the model is also given. The distribution shows that the cavity is easily formed near the wall at the shoulder of the projectile.

Regularity between the cavity and the vortex motion could be visualized based on the Q-criterion. The non-axisymmetric vertex around the projectile is generated by the collapse of the shedding cavity, which may affect cruising stability.

Wall effect in unsteady cloud cavitation is complex. Wall effect may change with varying distance between the near wall side and the wall nearby. The results reported in this study are limited to typical working conditions for a typically shaped model. Further in-depth analysis must be conducted in the future.

Acknowledgments

The authors would like to thank the National Natural Science Foundation of China through grant numbers 11202215, 11332011 & 11672315. This project was also supported by the Youth Innovation Promotion Association CAS (2015015).

References

[1] R.T. Knapp, J.W. Daily, F.G. Hammitt, Cavitation, McGraw-Hill, 1970.
[2] C.E. Brennen, Cavitation and Bubble Dynamics, Cambridge University Press, 2013.
[3] H. Ishida, C. Nuntadusit, H. Kimoto, T. Nakagawa, T. Yamamoto, Cavitation bubble behavior near solid boundaries, http://resolver. caltech. edu/cav2001: sessionA5. 003, 2001.
[4] H. Kimoto, K. Momose, H. Ueki, T. Onishi, A study of a cavitation bubble on a solid boundary, Bull. JSME 28 (1985) 601–609.
[5] X. Chen, C. Lu, J. Li, Z. Pan, The wall effect on ventilated cavitating flows in closed cavitation tunnels, J. Hydrodyn. Ser. B 20 (2008) 561–566.
[6] G. Chen, G. Wang, C. Hu, B. Huang, Y. Gao, M. Zhang, Combined experimental and computational investigation of cavitation evolution and excited pressure fluctuation in a convergent–divergent channel, Int. J. Multiph. Flow. 72 (2015) 133–140.

[7] J. Zhou, K. Yu, J. Min, M. Yang, The comparative study of ventilated super cavity shape in water tunnel and infinite flow field, J. Hydrodyn. Ser. B 22 (2010) 689–696.
[8] M. He, L. Yuan, L. Zhou, J. Yang, Z. Wang, Numerical evaluation of the side wall effect on the flow around a hydrofoil, Eng. Comput. 31 (2014) 501–509.
[9] T. Kida, Y. Miyai, Lift coefficients on a supercavitating jet-flapped foil between rigid walls, Bull. JSME 18 (1975) 151–158.
[10] T. Kida, Y. Miyai, Wall effect in cavitating flow past a thin jet-flapped foil, Quart. J. Mech. Appl. Math. 25 (1972) 83–103.
[11] O. Faltinsen, Hydrodynamics of high speed marine vehicles, in: Hydrodynamics VI: Theory and Applications: Proceedings of the 6th International Conference on Hydrodynamics, Perth, Western Australia, 24–26 November 2004, CRC Press, 2004, p. 3.
[12] O.M. Faltinsen, Y.A. Semenov, The effect of gravity and cavitation on a hydrofoil near the free surface, J. Fluid Mech. 597 (2008) 371–394.
[13] S. Bal, High-speed submerged and surface piercing cavitating hydrofoils, including tandem case, Ocean Eng. 34 (2007) 1935–1946.
[14] S. Bal, The effect of finite depth on 2D and 3D cavitating hydrofoils, J. Mar. Sci. Technol. 16 (2011) 129–142.
[15] S. Bal, S. Kinnas, A BEM for the prediction of free surface effects on cavitating hydrofoils, Comput. Mech. 28 (2002) 260–274.
[16] Y. Wang, X. Wu, C. Huang, X. Wu, Unsteady characteristics of cloud cavitating flow near the free surface around an axisymmetric projectile, Int. J. Multiph. Flow. 85 (2016) 48–56.
[17] Y. Wei, Y. Wang, F. Xin, C. Huang, Z. Duan, A scaled underwater launch system accomplished by stress wave propagation technique, Chin. Phys. Lett. 28 (2011) 024601.
[18] J.B. Leroux, O. Coutier-Delgosha, J.A. Astolfi, A joint experimental and numerical study of mechanisms associated to instability of partial cavitation on two-dimensional hydrofoil, Phys. Fluids (1994-Present) 17 (2005) 052101.
[19] H. Kanfoudi, H. Lamloumi, R. Zgolli, Numerical Investigation for Steady and Unsteady Cavitating Flows, INTECH Open Access Publisher, 2012.
[20] Q. Wu, B. Huang, G. Wang, Numerical simulation of transient flows around a 3D pitching hydrofoil, Adv. Mech. Eng. 7 (2015) 808034.
[21] X. Yu, C. Huang, T. Du, L. Liao, X. Wu, Z. Zheng, Y. Wang, Study of characteristics of cloud cavity around axisymmetric projectile by large eddy simulation, J. Fluids Eng. 136 (2014) 051303.
[22] R.E. Bensow, G. Bark, Implicit LES predictions of the cavitating flow on a propeller, J. Fluids Eng. 132 (2010) 041302.
[23] A. Gnanaskandan, K. Mahesh, Large eddy simulation of turbulent cavitating flows, in: Journal of Physics: Conference Series, IOP Publishing, 2015, p. 012135.
[24] C.P. Egerer, S.J. Schmidt, S. Hickel, N.A. Adams, Efficient implicit LES method for the simulation of turbulent cavitating flows, J. Comput. Phys. 316 (2016) 453–469.
[25] C.P. Egerer, S. Hickel, S.J. Schmidt, N.A. Adams, Large-eddy simulation of turbulent cavitating flow in a micro channel, Phys. Fluids (1994-Present) 26 (2014) 085102.
[26] M. Callenaere, J.P. Franc, J.M. Michel, M. Riondet, The cavitation instability induced by the development of a re-entrant jet, J. Fluid Mech. 444 (2001) 223–256.
[27] B. Ji, X. Luo, X. Peng, Y. Wu, H. Xu, Numerical analysis of cavitation evolution and excited pressure fluctuation around a propeller in non-uniform wake, Int. J. Multiph. Flow. 43 (2012) 13–21.
[28] R.F. Kunz, D.A. Boger, T.S. Chyczewski, D. Stinebring, H. Gibeling, T. Govindan, Multi-phase CFD analysis of natural and ventilated cavitation about submerged bodies, in: 3rd ASME/JSME Joint Fluids Engineering Conference, San Francisco, 1999, p. 1.
[29] F.M. Owis, A.H. Nayfeh, Numerical simulation of 3-D incompressible, multiphase flows over cavitating projectiles, Eur. J. Mech. B Fluids 23 (2004) 339–351.
[30] Y. Wang, C. Huang, T. Du, X. Wu, F. Xin, N. Liang, Y. Wei, Shedding phenomenon of ventilated partial cavitation around an underwater projectile, Chin. Phys. Lett. 29 (2012) 014601.
[31] X. Wu, Y. Wang, C. Huang, Effect of mesh resolution on large eddy simulation of cloud cavitating flow around a three dimensional twisted hydrofoil, Eur. J. Mech. B Fluids 55 (2016) 229–240.
[32] M.J. Berger, M.J. Aftosmis, S. Allmaras, Progress towards a Cartesian cut-cell method for viscous compressible flow, AIAA paper, 1301 (2012) 2012.
[33] C. Günther, D. Hartmann, L. Schneiders, M. Meinke, W. Schröder, A Cartesian cut-cell method for sharp moving boundaries, AIAA Paper, 3387 (2011) 27–30.
[34] A.K. Singhal, M.M. Athavale, H. Li, Y. Jiang, Mathematical basis and validation of the full cavitation model, Trans.-Amer. Soc. Mech. Eng. J. Fluids Eng. 124 (2002) 617–624.
[35] J. Kim, J. Holl, Water tunnel simulation study of the later stages of water entry of conical head bodies, in, DTIC Document, 1975.
[36] D. Stinebring, J. Holl, Water Tunnel Simulation Study of the Later Stages of Water Entry of Conical Head Bodies. Phase 2. Effect of the Afterbody on Steady State Ventilated Cavities, in, DTIC Document, 1979.
[37] P.J. Zwart, A.G. Gerber, T. Belamri, A two-phase on model for predicting cavitation dynamics, in: Fifth International Conference on Multi-phase Flow, Yokohama, Japan, 2004.
[38] X. Yu, Y. Wang, C. Huang, T. Du, Study on the influence of phase change rate on cloud cavitation, Procedia Eng. 61 (2013) 204–206.
[39] J. Sahner, T. Weinkauf, H.-C. Hege, Galilean invariant extraction and iconic representation of vortex core lines, in: EuroVis, 2005, pp. 151–160.